Journal of Hazardous Materials 463 (2024) 132893

Contents lists available at ScienceDirect

Journal of Hazardous Materials

journal homepage: www.elsevier.com/locate/jhazmat

Research Paper

The effect of synthesis conditions on the *in situ* grown MIL-100(Fe)-chitosan beads: Interplay between structural properties and arsenic adsorption

Jessy Joseph [a], Ari Väisänen [a], Ajay B. Patil [a,b], Manu Lahtinen [a,*]

[a] Department of Chemistry, University of Jyväskylä, P.O. Box 35, Jyväskylä FI-40014, Finland
[b] Helmholtz-Zentrum Dresden-Rossendorf (HZDR), Department of Process Metallurgy, Helmholtz Institute Freiberg for Resource Technology (HIF), Freiberg 09599, Germany

HIGHLIGHTS

- MIL-100(Fe) is *in situ* synthesized in chitosan solvogel beads for efficient sequestration of As^{3+} and As^{5+} .
- The adsorption performances of MIL-100(Fe)-chitosan composites are highly dependent on crystallinity.
- The crystallinity of the composites could be fine-tuned by carefully modulating the reaction parameters.
- MIL-100(Fe)-chitosan composites are highly selective towards arsenic.

GRAPHICAL ABSTRACT

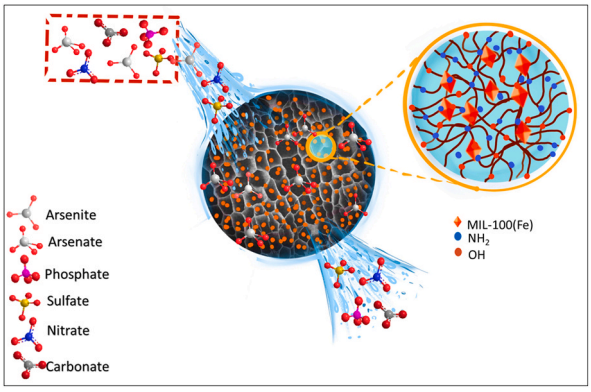

ARTICLE INFO

Editor: Arturo J Hernandez-Maldonado

Keywords:
Metal-organic frameworks
Aerogels
Hybrid materials
And crystallinity

ABSTRACT

Efficient sequestration of arsenic from drinking water is a global need. Herein we report eco-friendly porous hybrid adsorbent beads for removal of arsenic, through *in situ* synthesis of MIL-100(Fe) in the chitosan solvogel. To understand the structural *vs.* performance correlation, series of hybrid adsorbents were synthesized by modulating synthesis conditions like temperature, crystallization time, and concentration. Adsorbents were investigated using PXRD, FT-IR, SEM, and ICP-OES. Intriguing correlation between crystallinity and adsorption performance was observed as low and high crystalline MIL-100(Fe)-chitosan (ChitFe5 and ChitFe7, respectively) exhibited exceptional adsorption towards As^{5+} by removing it from water with 99% efficiency, whereas for As^{3+} species removal of about 85% was afforded. Adsorption isotherms indicated that increase in crystallinity (ChitFe5 -> ChitFe7), adsorption capacities of As^{5+} and As^{3+} increased from 23.2 to 64.5, and from 28.1 to 35.3 mg/g, respectively. Selectivity tests of the adsorbents towards As^{5+} and As^{3+} over competitive anions in the equimolar competitive systems having nitrates, sulfates, and carbonates demonstrated that the performance of the absorbents was fully maintained, relative to the control system. Through this study a highly selective and efficient adsorbent for arsenic species is designed and a clear insight into the structural tuning and its effect on adsorption performance is provided.

* Corresponding author.
E-mail address: manu.k.lahtinen@jyu.fi (M. Lahtinen).

https://doi.org/10.1016/j.jhazmat.2023.132893
Received 18 July 2023; Received in revised form 10 October 2023; Accepted 28 October 2023
Available online 31 October 2023

1. Introduction

Arsenic, a naturally occurring metalloid, is predominantly found in the Earth's crust and often accompanies various ores of metals such as copper, cobalt, nickel, and notably iron pyrite (FeS_2)[1]. Its release into the environment is facilitated by natural processes like the weathering of arsenic-rich rocks, floods, and volcanic activities. However, anthropogenic activities such as mining, agricultural practices, and metal smelting have accelerated the rate of its release, leading to growing international concerns about its hazardous impact on human health and other organisms[2]. Arsenic is recognized as an ecologically pervasive metalloid, affecting millions of people worldwide. The primary health risk associated with arsenic is its widespread impact on more than 220 million individuals globally[3]. The acceptable threshold for arsenic exposure is set at 10 μg/L but many affected areas report concentrations tens of micrograms higher than this level. Although exposure to arsenic can occur through various routes such as soil, air, and food, the most perilous form is through arsenic-contaminated water, particularly groundwater. This situation disproportionately affects developing countries. Groundwater contamination is commonly linked to geothermal processes, mineral dissolution, and reductive and oxidative desorption[4]. The consequences of arsenic exposure encompass a range of health hazards, with a significant emphasis on its classification as a human carcinogen, associated with the development of skin, lung, kidney, and bladder cancer [5,6]. The toxicity of arsenic is determined by its speciation, with inorganic forms, such as As^{3+} and As^{5+} containing oxyanions considered the most toxic. Effective elimination of arsenic from drinking water is an urgent requirement, especially in developing countries. Numerous technologies such as flocculation, precipitation, membrane filtration, chemical and biological oxidation as well as adsorption are adopted to mitigate arsenic[7]. However, for large-scale day-to-day applications, the chosen technique should be financially feasible, efficient, and intuitive. Adsorptive removal stands out as the most suitable technique for this purpose owing to the simple design and operation, and the possibility for regeneration and reuse of the spent adsorbents. Because of these merits, adsorption is employed mostly for treating arsenic-contaminated water in real-time use. The Garnet home-made filter and Magc-Alcan filter used in highly arsenic-prone regions of Bangladesh show the importance of adsorption[8]. Therefore, the development of more efficient adsorbents that could be directly employed for arsenic adsorption is indispensable.

Metal-organic framework (MOF), the porous coordination polymer is finding intense interest as an adsorbent in recent times. These materials can provide large range of functional opportunities by task-specifically selecting proper inorganic metal centers and organic linker(s) to design *e.g.*, water-stable adsorbent system with high porosity and surface area. Post-synthetic modification (PSM) of the formed network structure, and ease of functionalization of the organic linkers, can further enhance the competency of a MOF to act as a selective adsorbent. Due to the accessibility to open metal sites and high surface area, numerous studies have been reported depicting the role of MOF as an efficient adsorbent for arsenic[9,10]. Despite the advantages of MOFs, the ultrafine crystalline powders are not suitable for large-scale practical applications, as it leads to unfavorable situations of extreme aggregation, which in turn results in a reduced availability of active sites and performance. It will also generate difficulties in separating the adsorbent from the matrix and will generate secondary pollutants. It leads then to the compulsion of adding additional and complex separation steps. To tackle this limitation and to exploit the maximum potential of MOFs significant efforts are devoted in developing free-standing MOF monoliths, films, and membranes[11]. However, these materials are prone to structural degradation owing to their limited stability thus limiting their efficacy over time. Furthermore, the scalability of these materials is also a significant challenge[12]. To ensure scalability whilst maintaining financial sustainability, MOF-polymer composites are the best choice. Mostly MOF-polymer hybrid materials are formed by combining the distinctive properties of MOFs and synthetic polymers derived from petrochemicals. However, by considering the socio-economic effects and to ensure low carbon footprint, sustainable biopolymers are an optimal choice[13]. Several studies have investigated the combination of MOFs with biopolymers like cellulose alginate and agarose[14]. However, for the remediation of anionic pollutants the cationic chitosan, the second abundant biopolymer is one of the finest candidates[15,16].

Chitosan obtained by deacetylating of chitin is mostly found in the exoskeleton of crustaceans and contains abundant hydroxyl and amino groups. Combining chitosan and MOF to a hybrid material, can provide a significant improvement in the efficiency and selectivity of the anionic arsenic species recovery, because of the combined effects provided by the subcomponents. However, the simple blending of MOF particles with a chitosan matrix will generate difficulties due to the light-powdery nature of MOF, which may result in poor dispersion and agglomeration, consequently resulting in reduced surface area of the composite[17–19]. Likewise, the compatibility of the two phases also has an essential role to ensure strong interfacial interactions and thus ensuring the stability of MOFs within the matrix. These disadvantages could be overcome by synthesizing the MOFs *in situ* in chitosan[20–23]. The amine and hydroxyl groups in the chitosan are excellent anchoring sites for the metal cations, which can further be promoted into MOF structures by the introduction of organic ligands under appropriate reaction conditions.

Arsenic has a promising affinity towards iron, as a result, most of the established arsenic removal techniques are based on the utilization of iron-based complexes. Iron-based MOFs are also reported to be highly efficient for arsenic capturing. As per best of the author's knowledge this is one of the first studies regarding the utilization of chitosan-based *in situ* generated Fe-MOF composite for arsenic removal[24,25]. In this study, MIL-100(Fe) is *in situ* synthesized within the chitosan matrix, and the effect of synthesis conditions on the characteristics of the MIL-100 (Fe)-chitosan composite is investigated. Furthermore, a comprehensive examination is conducted to gain insight into the impact of crystal structure properties and different MOF concentrations on arsenic adsorption and removal.

2. Materials and methods

2.1. Materials

The source for Fe center, iron(III) nitrate nonahydrate ($Fe(NO_3)_3{\cdot}9\ H_2O$) was purchased from Sigma-Aldrich; the glacial acetic acid (100%) required for preparing chitosan solution; and hydrochloric acid (37%) for buffer preparation were purchased from VWR (AnalaR NORMAPUR ACS). The matrix-chitosan (from shrimp shells, ≥75% deacetylated), the organic ligand for MOF trimesic acid (H_3BTC, 98%), solvent for MOF synthesis, methanol, 2-amino-2-(hydroxymethyl)− 1,3-propanediol (Trizma® base) for buffer preparation were all received from Sigma-Aldrich. Concentrated nitric acid (>65%, used to prepare 5% nitric acid solutions required for Inductively Coupled Plasma Optical Emission Spectroscopy (ICP-OES)), was purchased from Honeywell Fluka. All chemicals were used as received without further purification and UHQ water was used throughout in synthesis and adsorption experiments, except on the real-life adsorption test conditions, wherein tap water was used.

2.2. Fabrication of MIL-100(Fe) embedded -chitosan adsorbent

MIL-100(Fe) was *in situ* generated in a chitosan matrix by following the methodology reported previously[23]. A chitosan-acetic acid colloidal solution was prepared by dissolving 9 mg/ml chitosan in 2% (v/v) of acetic acid solution. $Fe(NO_3)_3{\cdot}9\ H_2O$ of the desired concentration was introduced to the chitosan solution and stirred continuously until a homogenous chitosan-Fe solution was obtained. For the synthesis of chitosan beads with 2.6 mmol/g of metal content, 10 ml of chitosan colloidal solution was mixed with 0.23 mmol of $Fe(NO_3)_3{\cdot}9\ H_2O$. The

metal-complexed chitosan solution was added to 1 M NaOH solution in a dropwise manner. The instantaneously obtained beads were kept in the NaOH bath for 2 h with continuous stirring. The solidified beads were washed with water until the pH of the filtrate was neutral, followed by exchanging the solvent of the hydrogel for methanol, by immersing in a methanol-water solution with successively increasing the methanol concentration. Consequently, these solvogels were treated with a methanol solution of H_3BTC under specific solvothermal reaction conditions as given in Table 1. The concentration of H_3BTC:Fe was kept 1:1 throughout the reactions. The obtained MOF-chitosan beads were washed with methanol, followed by solvent exchange with water, and freeze-dried at − 50 °C overnight.

2.3. Characterization

The powder X-ray diffraction analyses (phase identification and crystallinity properties) of the obtained beads were made using Malvern Panalytical X'Pert PRO MPD powder X-ray diffractometer with Cu Kα radiation (λ = 1.5418 Å generated by sealed X-ray tube and Ni β-filter; 45 kV, 40 mA). Diffraction intensities were recorded in 2θ with the range of 3–50° by an X'Celerator position-sensitive detector. Data processing were carried out by the program X'Pert HighScore Plus (v. 4.9). The search-match phase identifications for the prepared crystalline phases were made in the same program using the simulated PXRD patterns (generated with Mercury program) of the expected reference single crystal structures that were retrieved from the Cambridge structural database (CSD)[26,27]. The chemical environment of the porous adsorbents was studied by Fourier transform infrared spectroscopy Nicolet iS50, (Thermo Fisher Scientific) in an ATR mode in the range 400–4000 cm^{-1}. The morphology analyses were performed using a scanning electron microscope (SEM, Zeiss EVO-50XVP) fitted with an energy-dispersive X-ray detector (EDX, Bruker Quantax 400). To determine Fe concentrations, the adsorbents were subjected to wet acid digestion using con. HNO_3 under ultrasound treatment and the obtained sample solution was subsequently analyzed using inductively coupled plasma-optical emission spectrometer (ICP-OES, Perkin Elmer Avio 500). To determine the point of zero charge, the pH drift method was used, and for that purpose 50 mg of the adsorbent was introduced to pH adjusted 0.1 M $NaNO_3$ electrolyte. A series of tests were carried out between the initial pH of 3–12, and the final pH were measured at 24 h.

2.4. Arsenic adsorption experiments

As^{3+} and As^{5+} stock solutions were prepared from As_2O_3 and $Na_2HAsO_4{\cdot}7\ H_2O$, respectively. The experimental solutions with desired concentrations were obtained by diluting the stock solutions using buffers of the desired pH. For all the adsorption tests, the MIL-100(Fe)-chitosan bead dosage was fixed as 1 g/L, and proper adsorbent analyte interaction was ensured by shaking the test solution at 280 rpm on a shaker. Adsorption kinetics were determined using 30 ml As^{3+}, and As^{5+} solutions, and a specific volume of aliquot was collected at regular intervals to determine the concentrations of arsenic species. Isotherm studies were carried out by varying concentrations of As^{3+}, and As^{5+} from 1 to 100 mg/L. Kinetic studies and isotherm studies were conducted for a contact time of 24 h. The effect of the pH on adsorption was investigated between pH 3–11, and for each test buffers of respective pH were prepared. Na_2CO_3, Na_2SO_4, $NaNO_3$, and Na_3PO_4 were used to test the effects of co-existing anions on arsenic adsorption. For studying the effect of pH and interfering anions, the adsorbent was shaken with arsenic solutions for 5 h. To investigate the reusability of the adsorbent, desorption-regeneration experiments were conducted. Initially, adsorbent was kept in contact with arsenic solutions for 6 h. Then the spent adsorbents were regenerated by soaking with 0.5 M $NaHCO_3$ for 6 h and the regenerated adsorbents were thoroughly washed with water to attain neutral pH and then reused in the next adsorption cycle, the process was repeated five times. Arsenic solutions with an initial concentration of 5 mg/L were used in all adsorption experiments. The concentrations of arsenic in the solutions before and after adsorption were assessed using ICP-OES, for the determination of adsorbed arsenic concentrations. The adsorption tests were conducted in duplicates, yielding results within an acceptable range of ± 5%.

The adsorption % and adsorption capacities (q_e) were calculated based on Eq. (1) and Eq. (2).

$$\text{adsorption}\% = \frac{C_o - C_e}{C_o} * 100 \quad (1)$$

$$\text{qe} = \frac{C_o - C_e}{W} * V \quad (2)$$

Where C_o and C_e (mg/L) are the initial and the equilibrium concentration of the analyte. V is the solution volume in liters and W is the dry mass of the adsorbent in grams.

Table 1
The specific experimental conditions for MIL-100(Fe)-chitosan composite.

Sample ID	Temp. (°C)	Time (h)	Solvent to solid ratio	Metal conc. (mmol/g)
ChitFe0				2.6
ChitFe1	120	5	1:1	2.6
ChitFe2	120	10	1:1	2.6
ChitFe3	120	15	1:1	2.6
ChitFe4	120	20	1:1	2.6
ChitFe5	80	20	1:1	2.6
ChitFe6	100	20	1:1	2.6
ChitFe7	140	20	1:1	2.6
ChitFe8	140	20	1:1	1.3
ChitFe9	140	20	1:1	5.2
ChitFe10	140	20	1:1	7.8

3. Results and discussion

3.1. Preparation and characterization

The synthesis procedure of adsorbents is depicted in Scheme 1. Fe-chitosan blend was introduced to the NaOH solution to fabricate instant hydrogel beads. They were subjected to react with trimesic acid to form MIL-100(Fe) embedded chitosan composite. Different composites were made by altering precursor dosage, crystallization time, and crystallization temperature to study the potential impact of reaction conditions on the resultant composites, with an emphasis on crystallinity. The initial concentration of Fe has been optimized for the instantaneous formation of resilient hydrogel beads upon introduction to NaOH, the further Fe-chitosan samples were prepared with 2x, 4x, and 6x loadings. In all synthesis procedures, the metal-to-ligand ratio was maintained at 1:1, and from ICP-OES analysis the Fe concentrations were determined as 56.88, 89.93, 138.29, and 150 mg/g. Fe-chitosan complex with 2x concentration was further utilized to explore the effects of crystallization temperature and crystallization time. Notably, all the resulting composites exhibited an average Fe content of 90 mg/g, implying that these parameters had no significant effect on the embedded metal concentration.

The PXRD patterns of *in situ* prepared MIL-100 (Fe)-chitosan beads at different crystallization temperatures, crystallization time, and metal concentrations are given in Fig. 1. The absence of the distinctively amorphous peaks of pure chitosan (see Fig. S1 in ESI) at 9.7°, and 20.4° 2θ ensures the development of hydrogel beads during the synthesis processes. Fig. 1a depicts the impact of temperature on the crystallinity of a composite material. The results reveal that temperature plays a crucial role in crystallinity. In the present study, the formation of MIL-100(Fe) within the chitosan matrix was confirmed by comparing the PXRD patterns obtained at 120 °C to the stimulated MIL-100 (Fe) pattern (CSD entry: CIGXIA)[28]. Through this study, MIL-100(Fe) was successfully synthesized within the chitosan matrix, in contrary to the

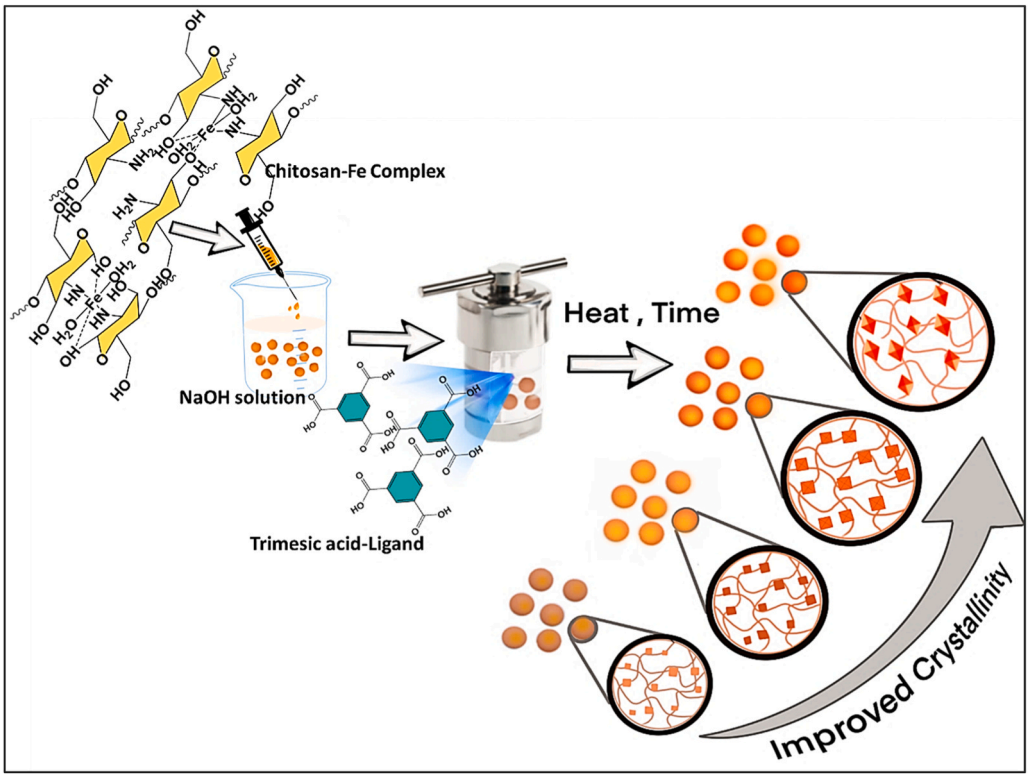

Scheme 1. Schematic representation of the synthesis process of MIL-100(Fe)-chitosan beads at different reaction parameters.

previous literature, which suggested the formation of semi-crystalline Fe-BTC at the same temperature[23]. Upon increasing the temperature to 140 °C the relative sharpness of the PXRD pattern is improved indicating enhanced crystallinity of the MIL-100(Fe). Whereas by reducing the temperature of synthesis process from 120 °C to 100 °C, the peak broadening is observed indicating diminishing crystallinity, crystal size, and an increase in the formation of crystal defects.

Nevertheless, the dominant MIL-100(Fe) phase remained crystalline, which was inferred by comparing the peaks at low angles around 4° 2θ, and the presence of a shoulder peak instead of broad single peak characteristic for semi-crystalline Fe-BTC at 11° 2θ. At lower temperature of 80 °C, a broad peak formation is observed that still correlates to the characteristic peak positions of MIL-100(Fe). However, the high broadening effect of the peak suggests that the framework is highly defective with small crystal size and low crystallinity. Additionally, the absence of any newly formed peaks corresponding to Fe-BTC, rules out its formation. These observations suggest that the MIL-100(Fe) framework undergoes substantial structural modifications with elevated temperatures. In addition, at lower temperatures defects and loss of crystallinity have been observed. Fig. 1b indicates the role of time on the crystal structure formation, when the temperature was kept constant at 120 °C, and the experimental time was varied from 5 to 20 h. The formation of MIL-100(Fe) is visible in the patterns within the first 5 h but with structural changes as mentioned above. However, with an increase in reaction time, the crystallinity also increased having the most crystalline phase resulted in 20 h treatment, as the PXRD pattern showed nearly all the characteristic peaks of MIL-100(Fe). Further investigation was carried out to understand the influence of precursor concentration on the *in situ* formation of MIL-100(Fe). It is apparent that loaded precursor concentration influences crystal formation. The PXRD patterns indicate that the initial concentration of Fe^{3+} was inadequate for the MIL-100(Fe) formation, as merely an amorphous broad peak centered at 4.4° 2θ was observed. On the other hand, the pattern is still completely different from the PXRD patterns of the Fe-chitosan complex (ChitFe0), which has no notable peaks (Fig. S1). This indicates that with the addition of ligand, nucleation for MIL-100(Fe) is initiated within the chitosan matrix but higher crystallinity and crystal size of MIL-100(Fe) structure is not attained. This may be because most of the Fe^{3+} ions in the chitosan matrix coordinate to the -OH and -NH_2 groups of chitosan, forming a cross-linked hydrogel, and thus are not available for forming a MOF structure. By doubling the Fe concentration, a pristine MIL-100(Fe) phase is formed within the hydrogel. On the PXRD pattern, this is manifested by narrow diffraction peaks indicating the presence of a crystalline phase. Thus, indicating that to obtain highly ordered MIL-100(Fe) framework phase, the concentration of Fe should be higher than the threshold concentration required to form the hydrogel. On further 4x and 6x increases in the concentration, the diffraction peaks in the measured PXRD patterns started to broaden. This could be caused by the fast-growth kinetics at higher precursor concentrations, which in turn generate higher crystal seeding and defect formation with the progress of crystal growth.

By analyzing the PXRD patterns we can assume that the most prominent influence on the crystal structure properties arises from temperature and precursor concentration. FT-IR was used to further analyze how these synthesis conditions affect to formation of the MIL-100(Fe) in the chitosan matrix (Fig. 2). It can be seen that measured PXRD patterns, and FT-IR spectra are highly correlated. A distinctive MIL-100(Fe) FT-IR spectra can be seen for all composites prepared at temperatures between 80 and 140 °C. On FT-IR spectra the signature peaks of MIL-100(Fe), which prominently arise from Fe-O, O-Fe-O are identified at 460 and 485 cm^{-1}, and the C-H bending vibrations of benzene ring are observed at 759 and 711 cm^{-1}. In addition, the peak corresponding to C-O bond vibration of carboxylate group is observed at 1619 cm^{-1}, and the symmetrical and asymmetrical vibration bands of O-C-O bonds are observed at 1385 and 1450 cm^{-1}, respectively[29,30]. Significant alterations in the intensity of the FT-IR signals occur when the temperature is increased from 80° to 140 °C. As the temperature elevates, there is a corresponding increase in the characteristic peak intensities. This observation is consistent with the PXRD data, revealing that more crystalline structures produce well-defined and intense FT-IR

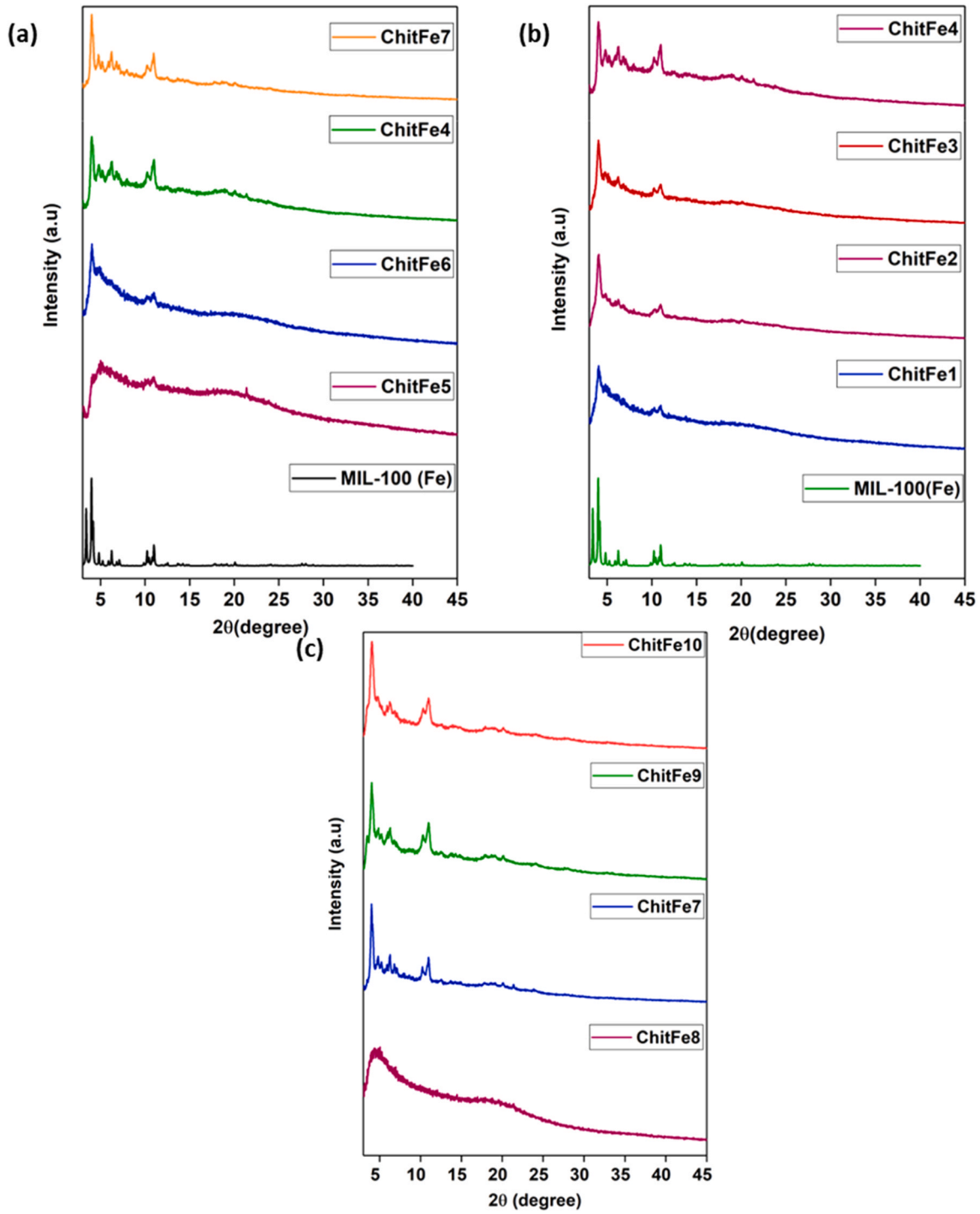

Fig. 1. PXRD patterns of MIL-100 (Fe)-chitosan composites obtained at different a) crystallization temperatures b) crystallization time and c) precursor concentration.

peaks, particularly at lower wavenumbers. Thus, FT-IR spectra could be considered as an indicator of crystallinity.

With more in-depth analysis of the weak and blurred FT-IR signals at 460 and 485 cm^{-1} corresponding to the low temperature preparations, we could anticipate that the low crystallinity relates to orderly dispositions of Fe clusters that generate non-uniformity in the COO-Fe environment of MIL-100(Fe). However, the absence of any new peaks eliminates the probability for a new chemical species to form in the matrix. The ChitFe0 composite sample exhibits peaks entirely different from composites with MIL-100(Fe). This further confirms that the Fe^{3+} coordinated in the chitosan matrix is converted to MIL-100(Fe) structure after the solvothermal reaction. The noticeable feature of MIL-100(Fe)-chitosan composite is that in comparison to the pristine chitosan microbeads the -NH band at 1650 cm^{-1} is absent in the composite beads. As well as the broad peak centered at 3380 cm^{-1} shows a significant decrease in intensity, which in turn ensures that ligation of chitosan to Fe centers occurred through -NH_2 and -OH functionalities. The effect of precursor concentration on the MIL-100(Fe) formation has been also further investigated using FT-IR spectroscopy, showing that the characteristic peak of Fe-O-Fe at 480 cm^{-1} is not observed at critical Fe-

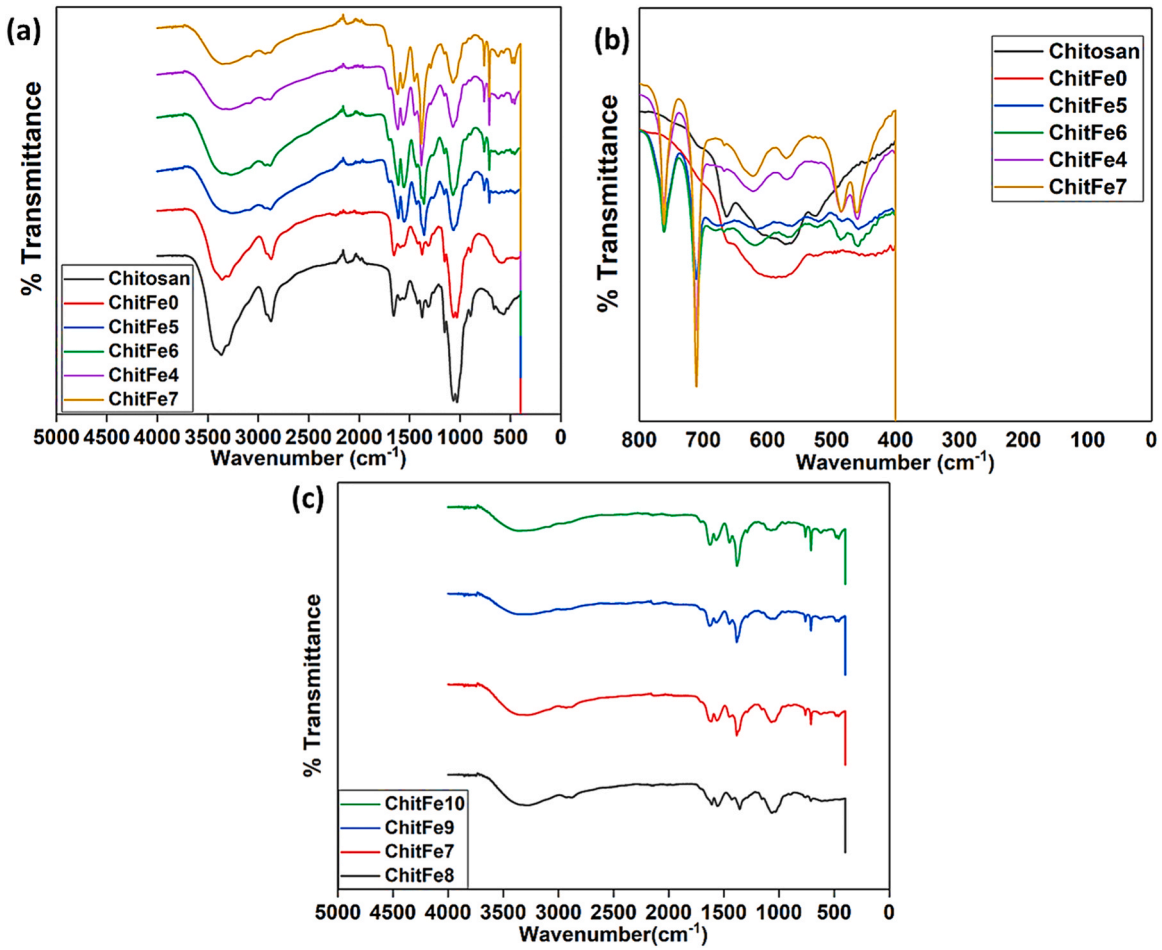

Fig. 2. a) FT-IR spectra of pure chitosan and MIL-100(Fe)-chitosan beads, b) the enlarged spectra from 400 to 800 cm^{-1}, and c) the effect of precursor concentration on the MIL-100(Fe)-chitosan beads.

concentration (ChitFe8). This is consistent with the PXRD results obtained. Upon doubling the concentration of the precursor, the Fe-O-Fe peak became evident. The peak intensity enhanced furthermore with 4x and 6x increase in concentrations, suggesting a greater abundance of Fe centers. An improvement in peak intensity at 1700 cm^{-1} is observed at higher precursor concentrations, which indicates the increase in the concentration of unreacted trimesic acid in the composite.

The SEM images of pure chitosan, ChitFe0, ChitFe5, and ChitFe7 beads are shown in Fig. 3. It could be observed that all the beads obtained in the present study are spherical and highly porous with honeycomb-like microchannel morphology. This hierarchical honeycomb structure is beneficial for the diffusion, interaction, and adsorption of arsenic, providing extensive MIL-100(Fe) active sites. The hierarchical structure of the chitosan aerogel is preserved for beads obtained at high thermal treatment, thus showing that the intertwined Fe-chitosan system is stable even at 140 °C. By closely observing the magnified SEM images, MIL-100(Fe) could be found even at the core of sphere, as shown in 10 μm magnified SEM image. This proves that the *in situ* method adopted in this study is successful in decorating the chitosan aerogel with MIL-100(Fe) throughout the matrix and the porous structure offers more surface for MIL-100(Fe) distribution as each microchannel act as a MIL-100(Fe) reservoir. As SEM images indicate, MIL-100(Fe) crystal particles are not agglomerated, which is an add-on property of *in situ* generation of functional adsorption sites in the polymer matrix. The formation of MOF particles is confirmed in ChitFe5 *i.e*, even at the lowest test temperature (80 °C). This further proves that the MIL-100(Fe) is formed in the chitosan matrix as evident in PXRD and FTIR.

3.2. Adsorption studies

ChitFe5 and ChitFe7 were employed for the adsorption tests of As^{3+} and As^{5+} species to extensively investigate the effect of crystal structure on the adsorption performance.

3.2.1. Adsorption kinetics

To determine the influence of the crystal structure on the adsorption rate and adsorption mechanism, the kinetic performance of ChitFe7 and ChitFe5 were evaluated. The kinetic investigation demonstrates that both ChitFe7 and ChitFe5 composite beads exhibit rapid adsorption of As^{5+} and As^{3+}, as about 50% of adsorption is complete within the first hour and an equilibrium is achieved within the duration of 6 h. The initial rapid adsorption rate could be explained by the fast diffusion of arsenic facilitated by the MIL-100(Fe) on the surfaces of the aerogel. The rapid rate of adsorption highlights the inherent advantage of the porous honeycomb morphology of the adsorbent, which enhances the area of adsorbent-adsorbate interaction. A further 50% of adsorption to reach equilibrium is performed by the embedded active sites of the adsorbents. Regardless of the differences in the structural properties both adsorbents exhibit similar adsorption performance for As^{5+} and could remove 99% of arsenic from the system. On the other hand, for the adsorption of As^{3+}, ChitFe5 displays slightly better adsorption performance with 93% removal efficiency, whereas ChitFe7 managed to attain 81% removal. To understand the adsorption pathways and the rate-determining mechanism involved, the obtained data is fitted with pseudo-first-order (Eq. 3) and pseudo-second-order (Eq. 4) kinetic models. The fitting curves are shown in Fig. 4 and fitting parameters are given in

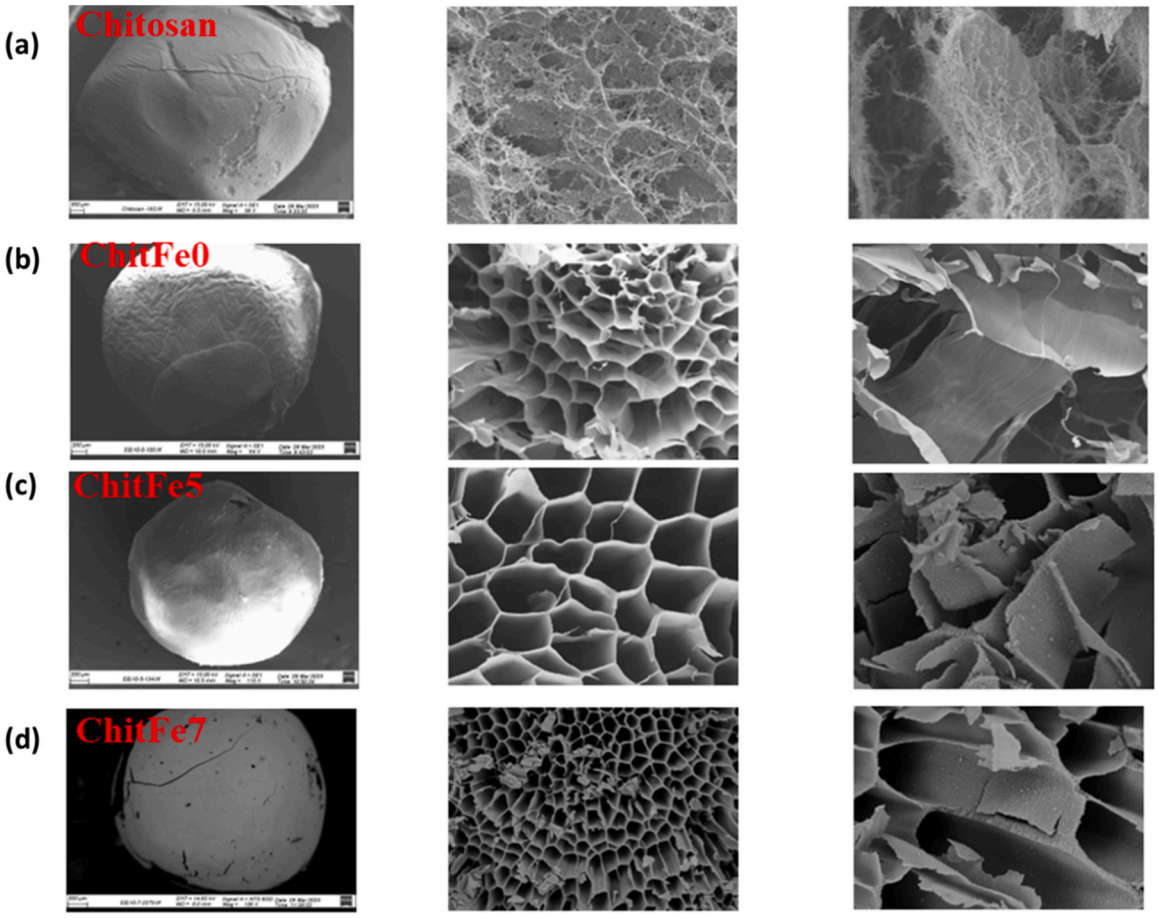

Fig. 3. SEM images of a) pure chitosan, b) ChitFe0, c) ChitFe5, and d) ChitFe7 beads and the corresponding cross-sections at 20 μm (middle) and 10 μm (right) range.

Table 2.

$$q_t = q_e(1 - e^{-k_1 t}) \quad (3)$$

$$q_t = \frac{k_2 q_e^2 \quad t}{1 + k_2 q_e t} \quad (4)$$

Where q_t (mg/g) is the adsorption capacity at the time t, $k_1(h^{-1})$ is the pseudo-first-order rate constant, k_2 (g/mg/h) is the pseudo-second-order rate constant. The fitted curves show that adsorbents ChitFe7 and ChitFe5 exhibit identical interactions and follow the same adsorption characteristics towards As^{3+} and As^{5+}. This indicates that the adsorption kinetics is not affected by the structural differences of the adsorbents. The pseudo-second-order model exhibits the perfect fit with an R^2 value exceeding 0.99, suggesting that the chemisorption of As^{3+} and As^{5+} is the rate-determining step for both adsorbents. In the early stages of adsorption, it could be seen that the pseudo-first-order model agrees with the experimental results. This supports the observation that the adsorbate undergoes quick diffusion and physisorption to the surface-active sites, though with time chemisorption overplays the adsorption rate. The rate constant for As^{5+} is similar for both adsorbents, but for As^{3+}, ChitFe7 shows a higher adsorption rate compared to ChitFe5. For further understanding of the adsorption properties, the trend and rate of intraparticle diffusion were studied with Weber-Morris model (Eq. 5).

$$q_t = k_d . t^{0.5} + L \quad (5)$$

Where q_t (mg/g) is the adsorption capacity at the time t, k_d is the intraparticle diffusion rate constant and L is the constant associated with interlayer thickness. Fig. 4c-f exhibits the intraparticle diffusion plots of q_t *versus* $t^{0.5}$ for ChitFe7 and ChitFe5 involved in the removal of As^{3+} and As^{5+}. Three distinct stages of adsorption are visible, the first rapid adsorption stage followed by gradual intra-particle diffusion and the final decelerated equilibrium state. The R^2 value obtained is lower in comparison to the second order kinetic model, and in any case the fitted line is not passing through the origin emphasizing that particle diffusion is not the only rate-determining mechanism. While comparing correlation coefficients of each individual stage (Table S1), the first stage of the adsorption process for the adsorbent shows higher R^2 values compared to the later stages, emphasizing the importance of diffusion in the initial period, which is predominated by chemisorption in the later stage.

3.2.2. *Adsorption Isotherms*

To evaluate the effect of arsenic concentration on adsorption and to calculate the maximum adsorption capacity of the ChitFe5 and ChitFe7, isotherm studies were carried out from concentrations ranging from 1 to 100 mg/L. From the analysis, it is evident that a positive correlation is maintained between concentration and adsorption capacity by both the adsorbents towards As^{3+} and As^{5+} species. While considering the lower concentrations of As^{5+} and As^{3+}, both ChitFe5 and ChitFe7 show promising prospects for reducing arsenic to microgram levels. The initial 1 mg/L of As^{5+} was reduced to 15 μg/L and 28 μg/L by ChitFe7 and ChitFe5, respectively. Similarly, both adsorbents could reduce initial 2 mg/L of As^{5+} to 27 μg/L and 50 μg/L, respectively. While for As^{3+}, ChitFe5 could reduce the initial 1 mg/L to 50 μg/L but not with ChitFe7. This shows that at alleviated concentrations the low crystalline ChitFe5 is equally efficient in removing As^{5+} and As^{3+}, whereas highly crystalline ChitFe7 is selective towards As^{5+}. Interestingly, as concentration increases ChitFe7 outperforms ChitFe5 in the removal of both forms of arsenic species. This indicates the crucial effect on performance due to the structural properties of the adsorbents. To further analyze the

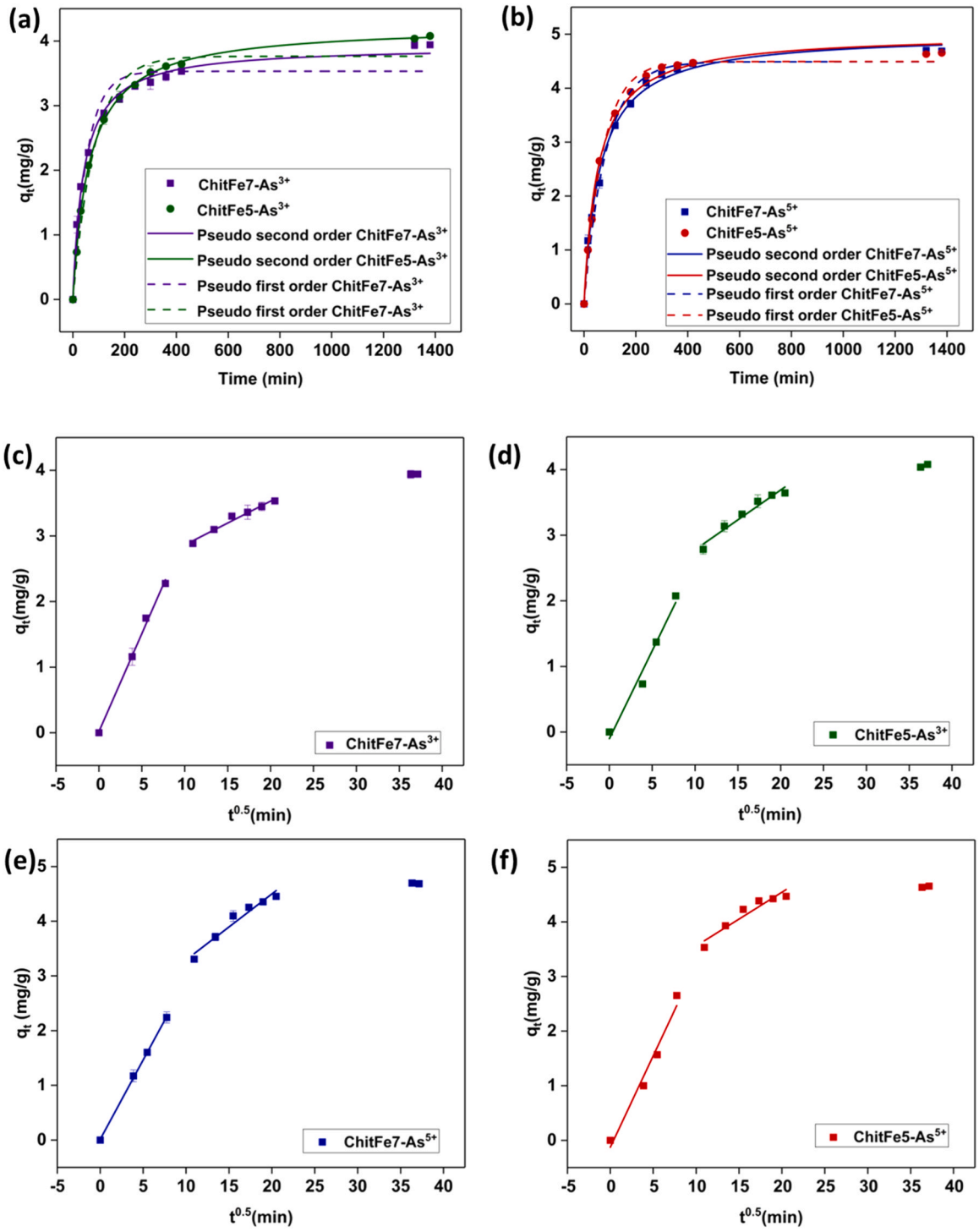

Fig. 4. The effect of time on the adsorptive removal of a) As^{3+}, and b) As^{5+} by ChitFe7 and ChitFe5 fitted with the pseudo-second order and pseudo-first order kinetic fitting models. Intraparticle diffusion model fitted to the adsorption behavior of c) ChitFe7 and d) ChitFe5 for As^{3+}, and e) ChitFe7, as well as f) ChitFe5 for As^{5+}. (Contact time = 24 h, adsorbent dosage = 1 g/L, initial concentration = 5 mg/L, As^{5+} pH = 7 and As^{3+} pH = 9).

adsorption behavior the isotherm data is fitted with Langmuir (Eq. 6) and Freundlich isotherm models (Eq. 7).

$$\frac{C_e}{q_e} = \frac{C_e}{q_m} + \frac{1}{k_L q_m} \tag{6}$$

$$q_e = k_f c_e^{\frac{1}{n}} \tag{7}$$

Where *Ce* is the concentration of arsenic remaining at adsorption equilibrium (mg/L), q_m and q_e represent the maximum adsorption capacity (mg/L) and equilibrium adsorption capacity, respectively. Langmuir constant related to binding energy is k_L and Freundlich constant related to the adsorption capacity is k_F. The nonlinear Langmuir and Freundlich isotherm fitting curves are depicted in Fig. 5, and isotherm parameters are given in Table 3. For As^{3+}, ChitFe5 exhibits a better fit with Freundlich adsorption isotherm ($R^2 > 0.9908$), whereas ChitFe7 fit best with Langmuir adsorption isotherm ($R^2 > 0.9951$). This indicates that As^{3+} favors multilayer adsorption on ChitFe5, and monolayer

Table 2
Data comparison of kinetic parameters of ChitFe7 and ChitFe5 for As^{3+} and As^{5+}.

	q_{exp} (mg/g)	Pseudo-first-order			Pseudo-second-order		
		q_e (mg/g)	K_1 (min^{-1})	R^2	q_e (mg/g)	K_2 (g/mg/min)	R^2
ChitFe7-As^{3+}	3.95	3.53	0.0183	0.9548	3.92	0.0061	0.9945
ChitFe5-As^{3+}	4.09	3.76	0.0118	0.9799	4.24	0.0036	0.9995
ChitFe7-As^{5+}	4.79	4.48	0.0117	0.9836	5.01	0.0032	0.9946
ChitFe5-As^{5+}	4.67	4.49	0.0137	0.9948	5.01	0.0037	0.9938

adsorption with ChitFe7. The q_m for the adsorption of As^{3+} by ChitFe7 is 35.25 mg/g, and 28.09 mg/g for ChitFe5, respectively. For As^{5+}, ChitFe5 shows a similar correlation with both Langmuir ($R^2 > 0.9445$) and Freundlich isotherm models ($R^2 > 0.9445$) resulting calculated q_m of 23 mg/g for ChitFe5. Whereas ChitFe7 exhibits exceptional adsorption capacity of $q_m = 64$ mg/g. The perfect fit with Freundlich adsorption isotherm ($R^2 > 0.9916$) could explain the exceptional adsorption of ChitFe7 possibly occurring through the multilayer adsorption. This is facilitated by the synergistic effect of the surface adsorption of As^{5+} on MIL-100(Fe), which further shifts the adsorption towards the pores of MIL-100(Fe) at higher concentrations. The q_m values of $As^{3+}$and $As^{5+}$for ChitFe5 and ChitFe7, respectively, exceed the reported q_m value for the Fe-chitosan complex, indicating the advantageous performance of MIL-100(Fe) embedded within the chitosan matrix[31]. ChitFe7 and ChitFe5 demonstrate efficiencies that are either comparable or higher than the values reported previously in the literature for As^{3+} and As^{5+} species recovering adsorbents (Table S2).

3.2.3. *pH variation studies*

The efficiency of adsorbent-adsorbate interaction is highly dependent on the pH of the aqueous solution and the surface charge of the adsorbent. By considering the high adsorption capacity manifested by ChitFe7 in comparison to ChitFe5, the effect of pH on the performance of ChitFe7 was investigated. In arsenic adsorption, pH is the key parameter due to the dependency of various oxidative forms of arsenic on pH as given in Table 4. The effect of pH on the point of zero charge (PZC) and on the arsenic adsorption is depicted in Fig. 6. Experimental results revealed that PZC of ChitFe7 is 4.27. Therefore, the adsorbent has a positive surface charge below pH 4 and is primarily negatively charged between pH 5–11. To understand the influence of pH on the adsorption

Table 3
Data comparison of isotherm parameters of ChitFe5 and ChitFe7 for As^{3+} and As^{5+}.

	Langmuir isotherm			Freundlich isotherm		
	q_m (mg/g)	k_L (L/mg)	R^2	K_f	n	R^2
ChitFe5 (As^{3+})	28.09	0.1457	0.9561	6.76	2.91	0.9908
ChitFe7 (As^{3+})	35.25	0.1336	0.9951	6.90	2.53	0.9293
ChitFe5 (As^{5+})	23.17	1.13	0.9445	10.40	4.16	0.9445
ChitFe7 (As^{5+})	64.45	0.17	0.9725	14.78	2.00	0.9916

performance of ChitFe7, As^{5+} and As^{3+} containing solutions between pH 3–11 were utilized. It can be noted that for As^{5+}, pH 7 is ideal for adsorption. The measurements showed an increase in adsorption from 28% to 94% between pH 5 and pH 7, then decreasing to 62% at pH 9, and finally to 35% at pH 11. In comparison to acidic pH, As^{5+} demonstrates better adsorption in alkali pH, as the pH rises from 5 to 7, As^{3+} also exhibits improved adsorption, thus increasing from 27% to 77%. The adsorption percentage gently rises until it reaches its maximum of 81.8% at pH 9, and then slightly decreasing to 80.7%, as the pH rises even higher to 11. In overall analyses indicate that adsorption is favored in neutral to alkaline pH for As^{3+} and As^{5+}. Since the adsorbent is effective at neutral pH, one of the key benefits of the hybrid material is that it requires no additional pH treatments to favor adsorption. Similarly to the effects of pH on aqueous solution, the temperature of the arsenic solution could affect the adsorption capacity of the adsorbent. Indeed, as Fig. S2 (see further analysis details in ESI) shows, the additional adsorption tests made in different arsenic solution temperatures indicated improved adsorption efficiency with an increase in the adsorption temperature, thus having the highest adsorption capacity at 50 °C and the lowest at 10 °C.

3.2.4. *Effect of anions on the adsorption*

The efficiency of the ion removal methods depends on the selectivity of the adsorbent towards arsenic species over the commonly present interfering anions. The influence of common anions like carbonates,

Table 4
Dominant arsenic species at different pH.

Arsenic species existing in water at different pH					
As^{5+}	H_3AsO_4	pH < 2	As^{3+}	H_3AsO_3	pH < 9
	$H_2AsO_4^-$	pH 2–7		$H_2AsO_3^-$	pH 9–12
	$HAsO_4^{2-}$	pH 7–11		$HAsO_3^{2-}$	pH 12–13
	AsO_4^{3-}	pH > 12		AsO_3^{3-}	pH > 13

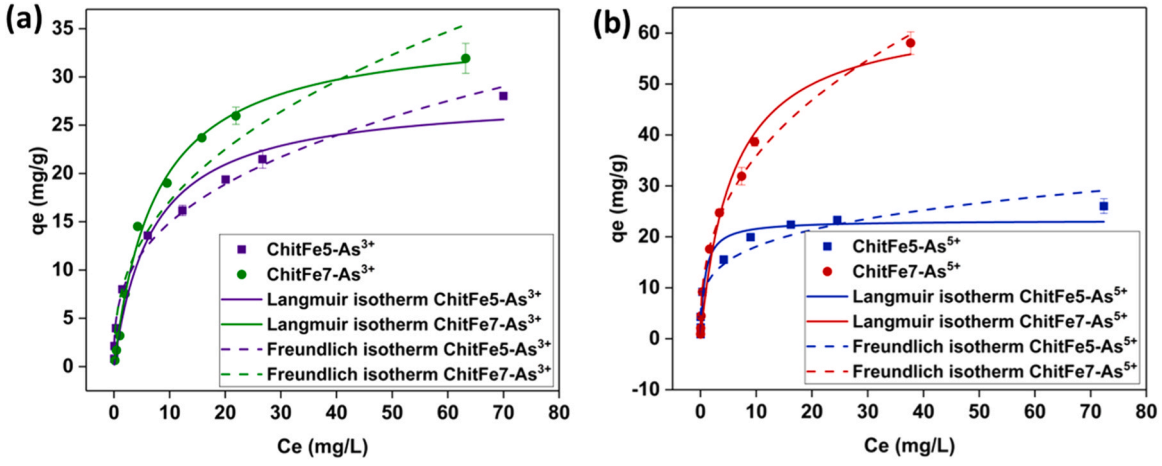

Fig. 5. The effect of concentration on the adsorptive removal of As^{3+} and As^{5+} by a) ChitFe5, and b) ChitFe7 fitted with the Langmuir and Freundlich adsorption isotherm models. (Contact time = 24 h, adsorbent dosage = 1 g/L, initial concentration = 1–100 mg/L, As^{5+} pH = 7 and As^{3+} pH = 9).

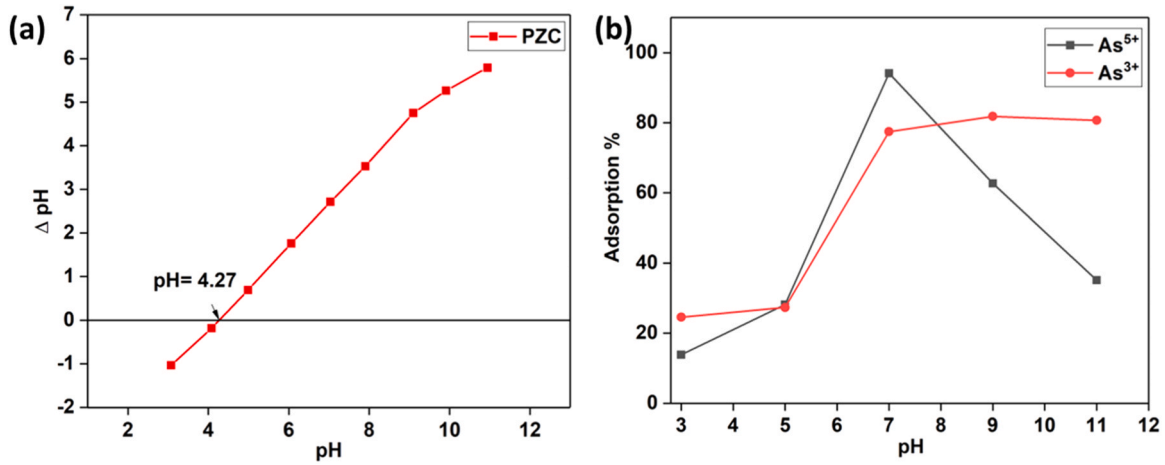

Fig. 6. a) The point of zero charge of the adsorbent ChitFe7, and b) effect of pH on the adsorption of arsenic by ChitFe7. (Contact time = 5 h, adsorbent dosage = 1 g/L, initial concentration = 5 mg/L, As^{5+} pH = 7 and As^{3+} pH = 9).

nitrates, sulfates, and phosphates were studied and depicted in Fig. 7. As these anions are commonly present, along with arsenic, in water resources studying their potential interference is crucial for possible practical applications. The interference of anions on As^{3+} and As^{5+} adsorption was studied at two concentrations. With an equimolar concentration of 5 mg/L and with a higher concentration of 10 mg/L, carbonates, nitrates, and sulfates showed absolute null interference toward the adsorption of As^{5+}. The adsorption capacity shows a slight decrease of 6.5% and 10.5% in the presence of phosphate at 5 and 10 mg/L, respectively. Similarly, the adsorption capacity for As^{3+} is also slightly affected by phosphate and sulfates but still in a system of 5 mg/L of phosphate and 10 mg/L of sulfates, the adsorbent maintains more than 90% removal capacity of As^{3+} in comparison to the control system. Due to similar atomic structure, complexation abilities with metal centers, as well as chemical properties of PO_4^{3-} and anionic arsenic species, phosphate is known to be the major interfering anion for the arsenic species. However, it seems that ChitFe7 has pronounced anti-interference ability and maintains about 90% selectivity towards As^{5+} and 85% selectivity towards As^{3+} even in the presence of higher phosphate concentrations.

3.2.5. *Effect of precursor concentration on the adsorption of Arsenic*

By modulating the precursor dosage, the MIL-100(Fe) loading in the adsorbent beads could vary and hence have a significant impact on the adsorption performance. To understand the effect of loading, MIL-100 (Fe)-chitosan beads prepared at different precursor concentrations were employed to adsorb As^{5+} and As^{3+}, and their performances are illustrated in Fig. 8. The ChitFe8, with a critical concentration of Fe^{3+} to form hydrogel, exhibits the least adsorption capability and shows similar adsorption for As^{5+} and As^{3+}. The ChitFe7, with doubled precursor concentration, exhibits 78% increase in As^{5+} adsorption and a 45% increase in As^{3+} adsorption. This steep surge in the adsorption performance could be attributed to the excellent adsorption capacity of MIL-100(Fe). The ChitFe9, with a four-fold increased precursor concentration, doesn't show significant enhancement in adsorption of As^{5+}, as merely 2% increase was observed, although for As^{3+} an 18% increase in adsorption was observed. Further enhancement in the precursor concertation deteriorated the overall adsorption performance, as ChitFe10 exhibits an 11% reduction in the As^{5+} removal, and for As^{3+} even higher reduction of 38% was observed. The abrupt reduction in the adsorption performance of ChitFe10 could be explained by the pore blockage and structural defects. The Fe concentration studies shows that ChitFe9 and ChitFe10 possess equivalent concentration of MIL-100(Fe). However, the FT-IR studies exhibit a higher intensity for the free carboxylic group peak at 1710 cm^{-1}, which indicates the presence uncoordinated organic ligand resulting in pore blocking. To gain a deeper understanding of the efficiency of MIL-100(Fe) loaded chitosan beads, comparative analyses were made involving ChitFe7, pristine chitosan beads, and MIL-100(Fe) bulk powder. Additionally, we employed ChitFe7 to extract As^{3+} and As^{5+} from solutions prepared in tap water (Fig. S3). Notably, pristine chitosan beads exhibited a mere 10% adsorption rate towards arsenic

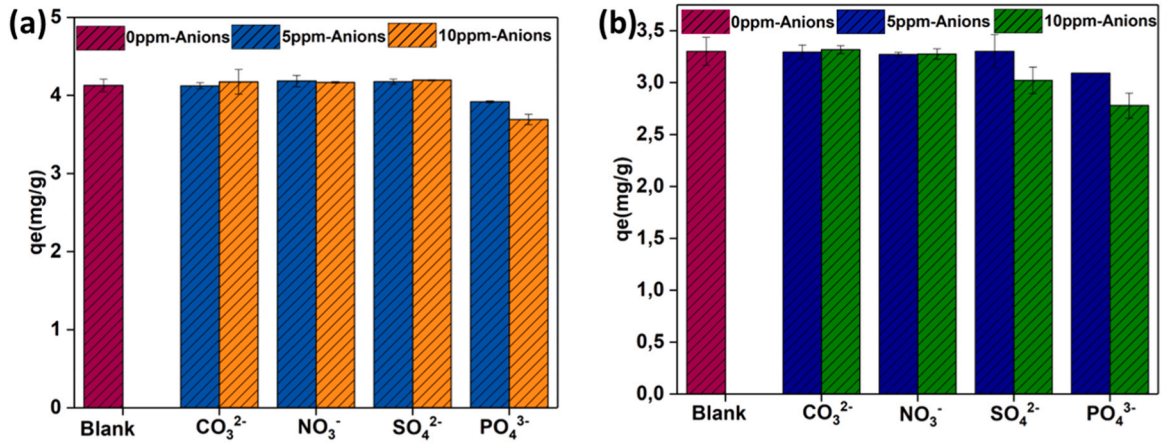

Fig. 7. The effect of anion interference on the adsorption of a) As^{5+} and b) As^{3+}. (Contact time = 5 h, adsorbent dosage = 1 g/L, initial concentration = 5 mg/L, As^{5+} pH = 7 and As^{3+} pH = 9, interfering anion concentrations = 5 and 10 mg/L).

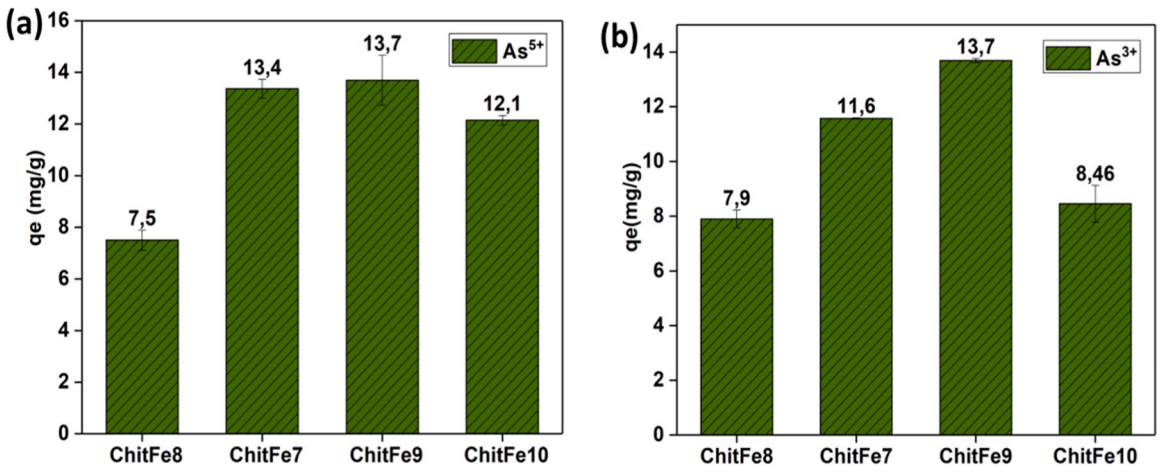

Fig. 8. The effect of precursor dosage on the adsorption of a) As^{5+} and b) As^{3+}. (Contact time = 5 h, adsorbent dosage = 1 g/L, initial concentration = 20 mg/L, As^{5+} pH = 7 and As^{3+} pH = 9).

species. Both MIL-100(Fe) and ChitFe7 demonstrated comparable performance, affirming that the composite formation process did not affect efficiency, in contrast it enhanced the efficiency but in terms of component usage, the ChitFe7 outperforms the pristine MIL-100(Fe) as similar or higher capacities can be afforded with considerably lower weight fraction of MOF. Moreover, bulk powders are very impractical to use as such, as an adsorbent. Finally, ChitFe7 maintained high performance in arsenic removal even from tap water solutions to which arsenic was added.

3.3. Regeneration Studies

The reusability and stability of the adsorbent in successive adsorption and desorption cycles are crucial parameters for real-life use. The successive adsorption cycles of ChitFe7 for As^{5+} and As^{3+} are depicted in Fig. 9. A facile decantation method was employed to separate the adsorbent from the adsorption media and the spent adsorbents were regenerated by 0.5 mol/L of $NaHCO_3$. It is worth noting that, as illustrated in Fig. S4a and b, the spherical ChitFe7 beads, recovered after the 5th regeneration cycle, have retained its physical integrity. A further analysis with SEM shows that the porous structure remained unaltered even after repeated adsorption and desorption cycles. This indicates the robustness of the adsorbent for continuous use (see further analysis details in ESI). In the case of As^{5+}, the adsorption capacity is constant till the first 3 cycles and then an equilibrium is achieved in the 4th and 5th cycles with a slightly reduced capacity. Compared to the 96% adsorption capacity in the first cycle the adsorbent maintained 85% removal efficiency in the 5th cycle. ChitFe5 shows adsorption behavior like the ChitFe7 in the first cycle. However, in the second cycle the adsorption capacity is already slightly more decreased than in case of ChitFe7, and the capacity is further decreased in the 3rd cycle. leveling to an equilibrium in the following two cycles. In overall, ChitFe5 show around 20% lower adsorption capacity compared to ChitFe7 (Fig. S5a) at 5th cycle. The efficiency of As^{3+} adsorption on ChitFe7 is reduced slightly after the first and second cycles but practically reaches equilibrium already in the 3rd cycle and maintains 60% adsorption level at the last 5th cycle. In comparison to As^{3+} the reusability of ChitFe7 is found better towards the removal of As^{5+}. The elution efficiency of As^{5+} and As^{3+} on ChitFe7 is given in Fig. S6, which indicates that As^{5+} could be eluted more efficiently from ChitFe7 than As^{3+}. This could also promote better performance of ChitFe7 towards As^{5+} than As^{3+} adsorption in successive cycles. In the case of ChitFe5 (Fig. S5b) the As^{3+}adsorption decreased in the successive cycles, as the 77% adsorption level for As^{3+} on pristine ChitFe5 was decreased to 48% in the second cycle, and in the 4th and 5th adsorption cycles the adsorption efficiency of ChitFe5 was decreased to roughly about half that of determined for ChitFe7. The reusability test confirms that enhancement in crystallinity improves the reusability of the adsorbent and is beneficial for overall performance.

4. Conclusion

In summary, a potential adsorbent for arsenic is synthesized *via in situ*

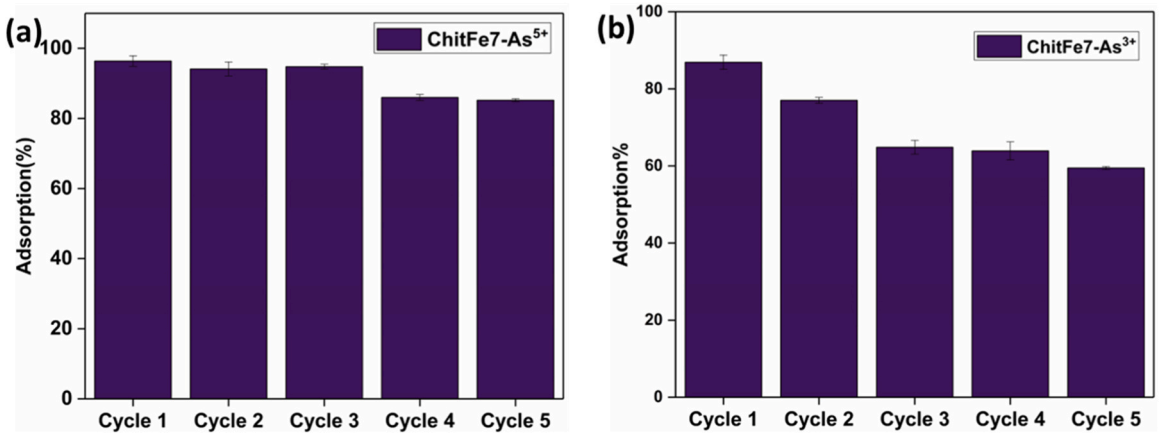

Fig. 9. The adsorption performance of ChitFe7 towards As^{5+} and As^{3+} in the consecutive cycles. (Contact time = 6 h, adsorbent dosage = 1 g/L, initial concentration = 5 mg/L, As^{5+} pH = 7 and As^{3+} pH = 9).

generation of MIL-100(Fe) in the chitosan matrix. The effect of key synthesis parameters, the crystallization temperature, time, and precursor concentration on the crystallinity of resulting composites were investigated. The PXRD and FT-IR analysis of the obtained honeycomb-structured microporous beads revealed that the crystallinity of the adsorbent could be significantly modulated by varying the synthesis conditions, especially the temperature. To understand the structural-performance correlation, the adsorbents with different crystallinity ChitFe5 and ChitFe7 were employed for As^{3+} and As^{5+} adsorption tests. The kinetic studies revealed that both adsorbents exhibit excellent removal efficiency of about 99% for As^{5+}. However, considering As^{3+}, ChitFe5 shows superior performance with a removal percentage of 93.6% compared to 81.7% achieved by ChitFe7. The adsorption kinetics of both the adsorbent towards As^{3+} and As^{5+} were well described by a pseudo-second order kinetic model with a remarkable correlation coefficient ($R^2 > 0.99$), revealing that the adsorption follows a chemisorption mechanism. Isotherm studies demonstrated a positive correlation between the crystallinity of the adsorbent and adsorption performance. As concentration increases the adsorption performance of ChitFe7 towards As^{5+} and As^{3+} outperforms ChitFe5. ChitFe7 exhibited a remarkable enhancement of 178.1% in adsorption capacity for As^{5+} in comparison to ChitFe5, while a noticeable enhancement of 25.4% was observed for As^{3+}. The selectivity of the adsorbent towards arsenic species in the presence of interfering anions is one of the most pronounced attributes of the synthesized adsorbent that could facilitate efficient practical utilization. At equimolar concentration nitrates, sulfate, and carbonates shows absolute nil interference in the adsorption of As^{5+} and As^{3+}. Phosphate slightly reduced the adsorption, however still in both systems, the adsorbent maintained about 94% of initial adsorption performance. The regeneration studies further confirmed the effect of structural properties of the MIL-100(Fe) on the adsorption performance, the improved crystallinity results in enhanced stability of the adsorbent in aqueous arsenic solution.

CRediT authorship contribution statement

Jessy Joseph as first author, has performed all the experimental work including syntheses and in most parts the characterization methods. Ari Väisänen and Manu Lahtinen have participated in supervision, assisting in material characterization (ICP-OES, PXRD) and for the ideation of the work. Ajay B. Patil has participated in designing adsorption test conditions and regeneration methods. All authors have participated to the writing and revision processes of the manuscript.

Environmental Implication

Arsenic is one of the elements with a threatening effect on human health from prolonged exposure even at acute concentrations. The major issue of concern with arsenic is that the prominent carrier of this deadly pollutant to the human body is drinking water. Developing countries like Bangladesh, India, and Ghana are the areas most affected by arsenic poisoning. Through this study, we design a new adsorbent with a high selectivity and adsorption capacity to mitigate arsenic content from aqueous systems. Moreover, we aimed to create a clear insight regarding the effects of the structural alterations on the adsorption capacity of the adsorbent.

Declaration of Competing Interest

The authors declare that they have no known competing financial interests or personal relationships that could have appeared to influence the work reported in this paper.

Data Availability

No data was used for the research described in the article.

Acknowledgments

This study was financially supported by the doctoral school program of the Department of Chemistry at the University of Jyväskylä, Finland.

Appendix A. Supporting information

Supplementary data associated with this article can be found in the online version at doi:10.1016/j.jhazmat.2023.132893.

References

[1] Raju, N.J., 2022. Arsenic in the geo-environment: a review of sources, geochemical processes, toxicity and removal technologies. Environ Res 203, 111782. https://doi.org/10.1016/j.envres.2021.111782.
[2] Rathi, B.S., Senthil Kumar, P., 2021. A review on sources, identification and treatment strategies for the removal of toxic Arsenic from water system. J Hazard Mater 418, 126299. https://doi.org/10.1016/j.jhazmat.2021.126299.
[3] Podgorski, J., Berg, M., 2020. Global threat of arsenic in groundwater. Science 368, 845–850. https://doi.org/10.1126/science.aba1510.
[4] Kumar, A., Ali, M., Kumar, R., Kumar, M., Sagar, P., Pandey, R.K., et al., 2021. Arsenic exposure in Indo Gangetic plains of Bihar causing increased cancer risk. Sci Rep 11, 2376. https://doi.org/10.1038/s41598-021-81579-9.
[5] Shameem, K., Abdul, M., Sammanthi Jayasinghe, S., Chandana, E.P.S., Jayasumana, C., Mangala, P., De Silva, C.S., 2015. Arsenic and human health effects: a review. Environ Toxicol Pharm 40, 828–846. https://doi.org/10.1016/j.etap.2015.09.016.
[6] Palma-Lara, I., Martínez-Castillo, M., Quintana-Pérez, J.C., Arellano-Mendoza, M. G., Tamay-Cach, F., Valenzuela-Limón, O.L., et al., 2019. Arsenic exposure: A public health problem leading to several cancers. Regul. Toxicol. Pharmacol. 10, 104539 https://doi.org/10.1016/j.yrtph.2019.104539.
[7] Alka, S., Shahir, S., Ibrahim, N., Ndejiko, M.J., Vo, D.V.N., Manan, F.A., 2021. Arsenic removal technologies and future trends: a mini review. J Clean Prod 278, 123805. https://doi.org/10.1016/J.JCLEPRO.2020.123805.
[8] Feenstra, L., Van Erkel, J., Utrecht, L.V., 2007. *Arsenic in groundwater: Overview and evaluation of removal methods*. Report nr. SP 2007-2,IGRAC P.O. In: Box, 80015. Utrecht The Netherlands, TA, p. 3508.
[9] Ramanayaka, S., Vithanage, M., Sarmah, A., An, T., Kim, K.H., Ok, Y.S., 2019. Performance of metal–organic frameworks for the adsorptive removal of potentially toxic elements in a water system: a critical review. RSC Adv 9, 34359–34376. https://doi.org/10.1039/C9RA06879A.
[10] Wang, C., Luan, J., Wu, C., 2019. Metal-organic frameworks for aquatic arsenic removal. Water Res. 158, 370. https://doi.org/10.1016/j.watres.2019.04.043.
[11] Kalaj, M., Bentz, K.C., Ayala, S., Palomba, J.M., Barcus, K.S., Katayama, Y., et al., 2020. MOF-Polymer Hybrid Materials: From Simple Composites to Tailored. Architectures, Chem. Rev. 120, 8267. https://doi.org/10.1021/acs.chemrev.9b00575.
[12] Jin, P., Tan, W., Huo, J., Liu, T., Liang, Y., Wang, S., Bradshaw, D., 2018. Hierarchically porous MOF/polymer composites via interfacial nanoassembly and emulsion polymerization. J Mater Chem A 6, 30. https://doi.org/10.1039/c8ta06766j.
[13] El Hankari, S., Bousmina, M., El Kadib, A., 2019. Biopolymer@Metal-Organic Framework Hybrid Materials: A Critical Survey. Prog. Mater. Sci. 106, 100579 https://doi.org/10.1016/j.pmatsci.2019.100579.
[14] Zhang, X.-F., Wang, Z., Ding, M., Feng, Y., Yao, J., 2021. Advances in cellulose-metal organic framework composites: preparation and applications. J. Mater. Chem. A 9, 23353. https://doi.org/10.1039/d1ta06468a.
[15] Keshvardoostchokami, M., Majidi, M., Zamani, A., Liu, B., 2021. A review on the use of chitosan and chitosan derivatives as the bio-adsorbents for the water treatment: Removal of nitrogen-containing pollutants. Carbohydr. Polym. 273, 118625 https://doi.org/10.1016/j.carbpol.2021.118625.
[16] Wang, X., Liu, Y., Zheng, J., 2016. Removal of As(III) and As(V) from water by chitosan and chitosan derivatives: a review. Environ Sci Pollut Res 23, 13789–13801. https://doi.org/10.1007/s11356-016-6602-8.
[17] Zhao, S., Li, Y., Wang, M., Chen, B., Zhang, Y., Sun, Y., et al., 2023. Efficient adsorption of Congo red by micro/nano MIL-88A (Fe, Al, Fe-Al)/chitosan composite sponge: preparation, characterization, and adsorption mechanism. Int J Biol Macromol 239, 124157. https://doi.org/10.1016/J.IJBIOMAC.2023.124157.
[18] Wang, Y., Wang, K., Lin, J., Xiao, L., Wang, X., 2020. The preparation of nano-MIL-101(Fe)@chitosan hybrid sponge and its rapid and efficient adsorption to anionic dyes. Int. J. Biol. Macromol. 1665, 2684 https://doi.org/10.1016/j.ijbiomac.2020.10.073.
[19] Musarurwa, H., Tavengwa, N.T., 2022. Advances in the application of chitosan-based metal organic frameworks as adsorbents for environmental remediation. Carbohydr Polym 283, 119153. https://doi.org/10.1016/j.carbpol.2022.119153.
[20] Zhu, X., Tong, J., Zhu, L., Pan, D., 2022. In situ growth of ZIF-8 on carboxymethyl chitosan beads for improved adsorption of lead ion from aqueous solutions. Int J Biol Macromol 205, 473–482. https://doi.org/10.1016/J.IJBIOMAC.2022.02.120.
[21] Zhang, Z., Hu, J., Tian, X., Guo, F., Wang, C., Zhang, J., et al., 2022. Facile in-situ growth of metal–organic framework layer on carboxylated nanocellulose/chitosan aerogel spheres and their high-efficient adsorption and catalytic performance. Appl Surf Sci 599, 153974. https://doi.org/10.1016/J.APSUSC.2022.153974.

[22] Ma, Y., You, D., Fang, Y., Luo, J., Pan, Q., Liu, Y., Wang, F., Yang, W., 2022. Confined growth of MOF in chitosan matrix for removal of trace Pb(II) from reclaimed water. Sep Purif Technol 294, 121223. https://doi.org/10.1016/J.SEPPUR.2022.121223.

[23] Zhao, R., Ma, T., Zhao, S., Rong, H., Tian, Y., Zhu, G., 2020. Uniform and stable immobilization of metal-organic frameworks into chitosan matrix for enhanced tetracycline removal from water. Chem Eng J 382, 122893. https://doi.org/10.1016/j.cej.2019.122893.

[24] Wei, Y., Zou, R., Xia, Y., Wang, Z., Yang, W., Luo, J., et al., 2022. Enhanced arsenite adsorption from water by activated MOF embedded in macroporous chitosan bionanocomposite beads. Mater. Today Chem. 26, 101091 https://doi.org/10.1016/j.mtchem.2022.101091.

[25] Zhang, S., Ding, J., Tian, D., 2022. Incorporation of MIL-101 (Fe or Al) into chitosan hydrogel adsorbent for phosphate removal: Performance and mechanism. J Solid State Chem 306, 122709. https://doi.org/10.1016/j.jssc.2021.122709.

[26] Gates-Rector, S., Blanton, T., 2019. The Powder Diffraction File: a quality materials characterization database. Powder Diffr. 34, 352. https://doi.org/10.1017/S0885715619000812.

[27] Macrae, C.F., Bruno, I.J., Chisholm, J.A., Edgington, P.R., McCabe, P., Pidcock, E., Rodriguez-Monge, L., Taylor, R., Van De Streek, J., Wood, P.A., 2008. Mercury CSD 2.0 – new features for the visualization and investigation of crystal structures. J Appl Crystallogr 41, 466–470. https://doi.org/10.1107/S0021889807067908.

[28] Horcajada, P., Surblé, S., Serre, C., Hong, D.-Y., Seo, Y.-K., Chang, J.-S., et al., 2007. Synthesis and catalytic properties of MIL-100(Fe), an iron(III) carboxylate with large pores. Chem. Commun. 27, 2820. https://doi.org/10.1039/b704325b.

[29] Chaturvedi, G., Kaur, A., Umar, A., Ajmal Khan, M., Algarni, H., Kumar Kansal, S., 2019. Removal of fluoroquinolone drug, levofloxacin, from aqueous phase over iron based MOFs,. MIL-100(Fe), J. Solid State Chem., 281, 121029. https://doi.org/10.1016/j.jssc.2019.121029.

[30] Lv, H., Zhao, H., Cao, T., Qian, L., Wang, Y., Zhao, G., 2015. Efficient degradation of high concentration azo-dye wastewater by heterogeneous Fenton process with iron-based metal-organic framework. J Mol Catal A Chem 400, 81–89. https://doi.org/10.1016/j.molcata.2015.02.007.

[31] Pincus, L.N., Petrovíčpetrovĭc, P.V., Gonzalez, I.S., Stavitski, E., Fishman, Z.S., Rudel, H.E., Anastas, P.T., Zimmerman, J.B., 2021. Selective adsorption of arsenic over phosphate by transition metal cross-linked chitosan. Chem Eng J 412, 128582. https://doi.org/10.1016/j.cej.2021.128582.